JGR Atmospheres

RESEARCH ARTICLE
10.1029/2018JD029586

Characteristics of Sea-Effect Clouds and Precipitation Over the Sea of Japan Region as Observed by A-Train Satellites

Tyler K. West[1], W. James Steenburgh[1], and Gerald G. Mace[1]

[1]Department of Atmospheric Sciences, University of Utah, Salt Lake City, UT, USA

Abstract Prolific winter (December-January-February) snowfall occurs over northwest Japan due to frequent sea-effect precipitation that develops during cold-air outbreaks over the Sea of Japan (SOJ). Knowledge of sea-effect clouds and precipitation across the SOJ region has historically been constrained, however, by limited offshore in situ observations and remote-sensing limitations. This paper uses sensors from National Aeronautics and Space Administration (NASA)'s A-Train Satellite Constellation to examine winter sea-effect properties in the SOJ region. The analysis shows that cloud and precipitation occurrence generally increases across the SOJ from Asia to Japan, as potential sea-effect periods with an along-orbit mean sea surface to 850-hPa temperature difference ≥13 °C comprise a majority of the total clouds and precipitation. Sea-effect clouds and precipitation occur most frequently in an arc-shaped area that extends from the western SOJ, where the Japan-Sea Polar-Airmass Convergence Zone (JPCZ) is common, to the coast of Honshu, and then northward to Hokkaido. Radar, lidar, and column water path statistics along A-Train orbital tracks show that sea-effect precipitation is deepest along the central Honshu coast and becomes shallower but more frequent with northward extent. Precipitation amount and frequency maximize along the coast and adjacent mountains but decline with inland extent, most abruptly downstream of higher mountain barriers. This work illustrates that air-sea interactions, coastal geometry, and regional topography strongly modulate cloud and precipitation patterns during sea-effect periods in the SOJ region.

Key Points:
- The majority of winter clouds and precipitation over the Sea of Japan region occur during sea-effect periods
- The distribution of sea effect varies in the region and is modulated by land-sea interactions, coastline geometry, and orographic effects
- Sea-effect precipitation is shallower and more common (deeper and less common) in the northern (southern and central) Sea of Japan region

Correspondence to:
T. K. West,
tyler.k.west@utah.edu

Citation:
West, T. K., Steenburgh, W. J., & Mace, G. G. (2019). Characteristics of sea-effect clouds and precipitation over the Sea of Japan region as observed by A-Train satellites. *Journal of Geophysical Research: Atmospheres*, *124*, 1322–1335. https://doi.org/10.1029/2018JD029586

Received 30 AUG 2018
Accepted 10 JAN 2019
Accepted article online 15 JAN 2019
Published online 7 FEB 2019

1. Introduction

Copious amounts of snow fall each cool season over land areas downstream of the Sea of Japan (SOJ), creating some of the largest seasonal snowfalls and deepest seasonal snowpacks in the world (Takahashi et al., 2013; Yamaguchi et al., 2011). Heavy snowstorms frequently impact the northwest Japanese coast and adjacent topography, disrupting transportation, contributing to structural damage and periods of elevated avalanche risk, and building a snowpack critical for regional water resources and winter tourism (Chechin & Pichugin, 2015; Eito et al., 2005; Nakai et al., 2012; Steenburgh, 2014). Much of this snowfall results from sea-effect precipitation (e.g., Campbell et al., 2018; Eito et al., 2010; Magono et al., 1966; Mizukoshi, 1977; Murakami et al., 1994; Nakai et al., 2005; Tsuchiya & Fujita, 1967), a phenomenon closely related to lake-, sea-, and ocean-effect precipitation in other regions of the world (e.g., Andersson & Nilsson, 1990; Kindap, 2010; Kristovich et al., 2017; Laird et al., 2009; Niziol et al., 1995; Norris et al., 2013; Steenburgh et al., 2000; Veals & Steenburgh, 2015). Sea effect over the SOJ occurs predominantly during the East Asian winter monsoon, which results from the interaction of the semipermanent Siberian High over northern Asia and the Aleutian Low in the Gulf of Alaska and features mean northwesterly flow over the SOJ during winter (Boyle & Chen, 1987; Dorman et al., 2004). Concomitant cold-air outbreaks (Mitnik, 1992) gain heat and moisture over the relatively warm waters of the SOJ and Tsushima current, destabilizing the atmosphere and generating clouds and precipitation (e.g., Hozumi & Magono, 1984; Tsuchiya & Fujita, 1967). Sea-effect precipitation systems then reach the northwest Japanese coast, where they are modified by coastal, inland, and orographic effects (e.g., Campbell et al., 2018; Estoque & Ninomiya, 1976; Kawamoto et al., 1963; Kusunoki et al., 2005; Nakai & Endoh, 1995; Saito et al., 1996; Yoshihara et al., 2004).

Previous studies have focused on sea effect in portions of the SOJ region but have been limited in geographic extent. Specific efforts to describe the precipitation distribution near Japan illustrate an increase in precipitation from the SOJ to the Japanese coast and mountains. Examples include Estoque and Ninomiya (1976), who present figures showing mean daily liquid precipitation equivalent during winter 1965 increasing from ~1–2 mm/day over the coastal SOJ to 4–7 mm/day over northwest Japan. Using regional modeling,

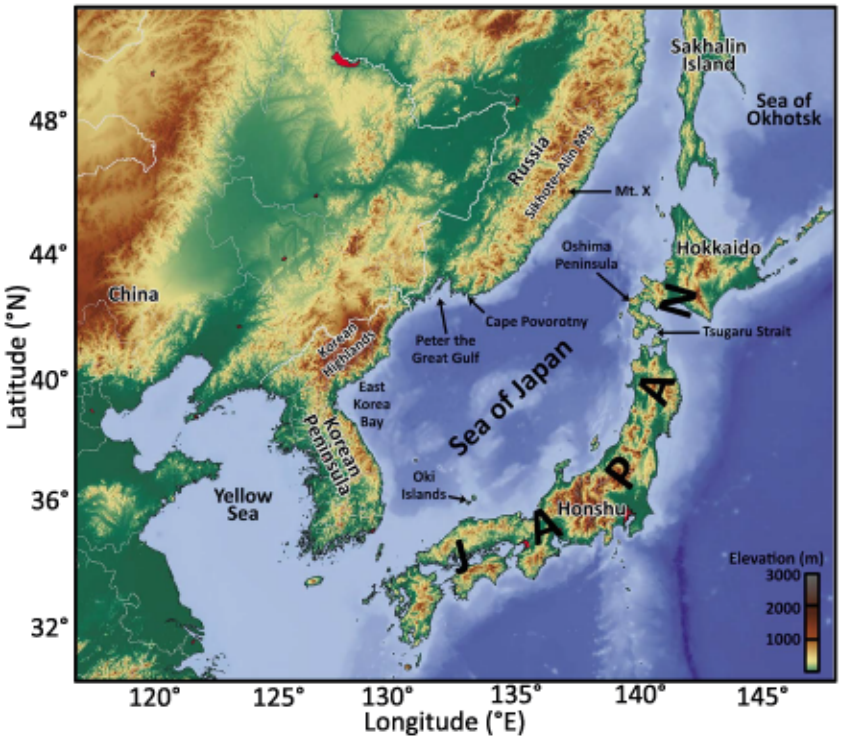

Figure 1. Topography of East Asia and Japan. Terrain elevation (m mean sea level) color filled as in scale. The red color fill represents major urban areas. Adapted from maps-for-free.com.

Takahashi et al. (2013) found an increase in simulated liquid precipitation equivalent from ~50–100 mm/month over the near-coast SOJ to ~300–400 mm/month over the adjacent Japanese mountains. Important variations in the distribution of precipitation occur, however, from case to case. For example, Magono et al. (1966) distinguish between *Satoyuki* storms, which produce heavier lowland snowfalls, and *Yamayuki* storms, which produce heavier mountain snowfall, while Nakai et al. (2005) identify a wide range of snowfall modes that influence the distribution and intensity of snowfall.

Research over the SOJ has identified three areas of frequent flow convergence and enhanced cloudiness and precipitation, although their climatological contributions to clouds and precipitation have not been quantified. The first is the Japan-Sea Polar-Airmass Convergence Zone (JPCZ), which forms due to flow interactions with the Korean Highlands just north of the Korean Peninsula (see Figure 1 for geographic locations), the thermal contrast between the Korean Peninsula and SOJ, and the sea surface temperature distribution of the SOJ (Nagata, 1987, 1991; Nagata et al., 1986). The JPCZ normally originates near the base of the Korean Peninsula and extends toward the Japanese coast, but its termination location can vary between ~133°E and ~139°E (Eito et al., 2010). The second area of convergence occurs in the northern SOJ to the lee of elevated near-coast topography in the Sikhote-Alin Mountains of eastern Russia, with the attendant cloud band usually extending eastward to Hokkaido (Muramatsu, 1979; Ohtake et al., 2009.) Following Ohtake et al. (2009), we refer to this as the Mt. X region. The third area of convergence occurs in the northern SOJ when northwesterly flow from Asia converges with northeasterly flow from the Sea of Okhotsk just west of Hokkaido and Sakhalin Island (Katsumata et al., 1998). Although oriented quasi-meridionally, the southern end of this convergence zone and its associated cloud band can curve eastward and intersect Hokkaido.

The purpose of this paper is to take advantage of spaceborne remote sensors carried by National Aeronautics and Space Administration (NASA)'s A-Train satellite constellation (Stephens et al., 2002) to describe the characteristics of sea-effect clouds and precipitation in the SOJ region. The data and methods used are described in section 2. Regional results regarding the occurrence of clouds and precipitation during winter (December-January-February [DJF]) and concomitant potential sea-effect periods (hereafter PSEPs) are presented in section 3. Section 4 centers on cross sections of PSEP reflectivity along

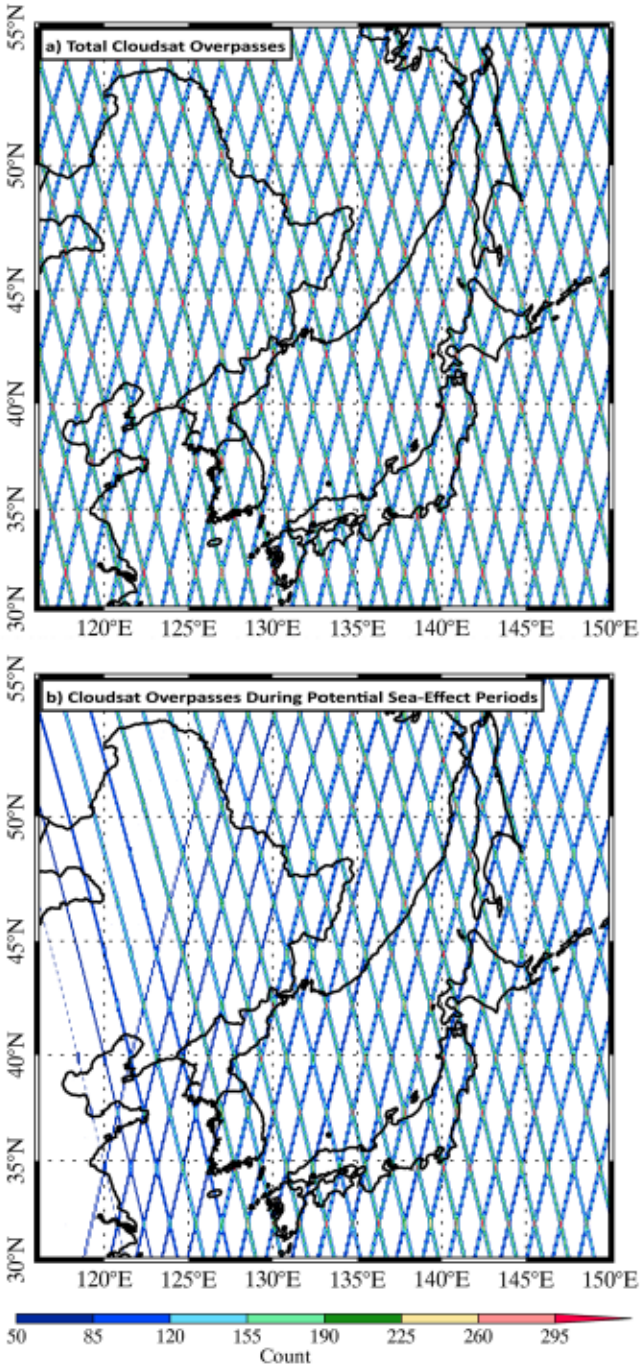

Figure 2. (a) Number of Cloudsat profiles with data available from Jan 2007 to Feb 2014. (b) Number of Cloudsat profiles with data available during potential sea-effect periods. The color-filled pixels are larger than the actual Cloudsat footprint to show numerical values, which can depict an artificial fluctuation in neighboring values.

individual Cloudsat tracks, while section 5 analyzes column water paths along these same Cloudsat tracks. Conclusions and avenues for future work are summarized in section 6.

2. Data and Methods

The primary instruments used for this study are NASA's cloud profiling radar (CPR) onboard the Cloudsat satellite and the Cloud-Aerosol Lidar with Orthogonal Polarization (CALIOP) onboard the CALIPSO satellite. Cloudsat and CALIPSO are polar-orbiting, Sun-synchronous satellites that fly in close formation at an altitude of ~705 km and cross the equator at ~0130 and ~1330 local solar time, with orbital tracks separated by ~95–145 km in the SOJ region (Figure 2a). The CPR is a nadir-pointing 3-mm wavelength (94 GHz) radar with an ~1.7-km along-track footprint, ~1.4-km cross-track footprint, 240-m vertical range bins, and an approximate −30-dBZ minimum detectable signal (Im et al., 2005; Tanelli et al., 2008). CALIOP's 20-ns laser pulse results in a 70-m footprint, with averaging producing 30-m vertical resolution (Winker et al., 2003). We focus on winter months (DJF) from January 2007 to February 2014, with data unavailable during January 2011 and from December 2011 to February 2012. Due to a battery anomaly, data from the night orbital tracks (descending from NE to SW; Figure 2a) are unavailable after April 2011. This results in a daytime data bias, but visual inspection of statistics derived using day versus night orbital tracks prior to April 2011 yielded small qualitative differences.

Total cloud occurrence is defined as the ratio of profiles (i.e., Cloudsat footprint volumes) with cloud detections to all profiles. Detections were based on the existence of one or more cloud layers within a profile as identified by the CloudSat Radar-Lidar-Geometrical Profile Product (2B-RL-GEOPROF; Mace & Zhang, 2014), which utilizes CALIOP's ability to detect thin clouds (often missed by the CPR) and the CPR's ability to observe lower cloud layers (often missed by CALIOP due to attenuation; Mace et al., 2009]. Total precipitation occurrence is defined as the ratio of profiles with surface precipitation to all profiles, with surface precipitation based on the CloudSat 2C-PRECIP-COLUMN product (hereafter 2C-PRECIP; Haynes et al., 2009]. For plan view plots of total cloud occurrence and other variables, available winter profiles along orbital tracks were compiled into 1° × 1° latitude-longitude grid boxes (e.g., Kulie et al., 2016; Mace et al., 2009) and smoothed using a boxcar average with a width of 3.

We also examine cloud and precipitation characteristics during PSEPs. To identify PSEPs, we calculate the sea surface to 850-hPa temperature difference, $\Delta T_{sea\text{-}850}$, for each Cloudsat profile using ECMWF temperature data from Cloudsat's 2C-PRECIP (Haynes et al., 2009) and ECMWF-AUX (Igel et al., 2014; Partain, 2007) products and only use overpasses with an along-orbit, basin-averaged sea surface to 850-hPa temperature difference, $\overline{\Delta T}_{sea\text{-}850}$, ≥13 °C over the SOJ, Yellow Sea, East China Sea, or Sea of Okhotsk, or Pacific Ocean (Figure 2b). For overpasses crossing both the SOJ and Pacific Ocean basins, we consider only the SOJ $\overline{\Delta T}_{sea\text{-}850}$.

The 13 °C threshold is commonly used as the minimum required for lake-effect precipitation over the Laurentian Great Lakes (Holroyd, 1971; Niziol, 1987; Niziol et al., 1995). This threshold approximately represents a dry adiabatic lapse rate, with higher values likely associated with an unstable boundary layer

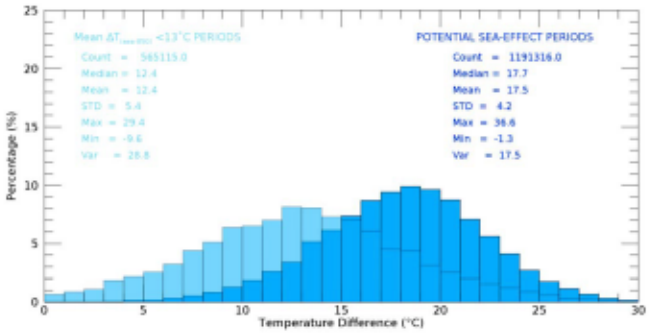

Figure 3. Histograms of individual Cloudsat profiles in which the overpass mean sea-surface to 850-hPa temperature difference, $\overline{\Delta T}_{\text{sea-850}}$, is <13 °C (light blue) and, $\overline{\Delta T}_{\text{sea-850}}$, is ≥13 °C (dark blue). The latter represent potential sea-effect periods.

over water (Niziol et al., 1995), and identifies overpasses in which thermodynamic conditions supporting sea effect exist along at least a portion but not necessarily all of the overpass. The 13 °C threshold shifts the distribution of clouds sampled to those occurring with a large $\Delta T_{\text{sea-850}}$ (Figure 3). For example, 87% of the overwater profiles during PSEPs feature a $\Delta T_{\text{sea-850}} \geq 13$ °C, with a median of 17.7 °C. In contrast, only 46% of the overwater profiles during other periods feature a $\Delta T_{\text{sea-850}} \geq 13$ °C, with a median of 12.4 °C. Some overpasses include individual profiles with $\Delta T_{\text{sea-850}} < 13$ °C and although we could have removed these profiles, this created ambiguities about how and when to add or remove profiles in adjacent overland areas where $\Delta T_{\text{sea-850}}$ could not be calculated. Thus, we have elected to include all profiles from overpasses with $\overline{\Delta T}_{\text{sea-850}} \geq 13$ °C as PSEPs. Results for individual over-water profiles with $\Delta T_{\text{sea-850}} \geq 13$ °C were compared to results for overpasses with $\overline{\Delta T}_{\text{sea-850}} \geq 13$ °C, and no major qualitative differences were found (not shown). In addition, although some non-sea-effect clouds may produce precipitation when $\overline{\Delta T}_{\text{sea-850}} \geq 13$ °C, studies indicate that most of the precipitation falling on the west coast of Japan during DJF is produced by clouds generated over the SOJ (e.g., Nakai et al., 2005).

Figure 4 presents examples for three overpasses crossing the Honshu coast near the city of Joetsu overlaid on visible Moderate Resolution Imaging Spectroradiometer (MODIS) imagery from the Aqua satellite. The first example features a large $\overline{\Delta T}_{\text{sea-850}}$ of 29.8 °C (Figure 4a), which would likely lead to a strongly unstable boundary layer (Niziol et al., 1995). Sea-effect clouds occur across nearly the entire SOJ, with a pronounced band downstream of the Mt. X region and bands in the JPCZ region. The CPR shows echo tops increasing from ~1,,800 m near the coast of Asia to ~2,800 m near the Honshu coast. Cloud amount decreases rapidly with inland extent where high terrain exists over Honshu and Hokkaido, although there is more cloud coverage downstream of Oshima Peninsula, Tsugaru Strait, and northern Honshu where the terrain is less formidable. The second example features a moderate $\overline{\Delta T}_{\text{sea-850}}$ of 18.6 °C with less cloud cover over the SOJ and fewer sea-effect cloud bands (Figure 4b). Cloud processes are more difficult to infer, with the CPR showing deeper echo tops compared to Figure 4a and distinct areas of higher reflectivity over the central SOJ and Japanese SOJ coast. In contrast, the third example features a low $\overline{\Delta T}_{\text{sea-850}}$ of 8.8 °C with a low-pressure system centered over the northern SOJ (Figure 4c). CPR echoes near the Asian coast are associated with synoptic and potentially orographic forcing, with similar clouds also found near the Honshu coast. Some sea-effect clouds are evident in the wake of the synoptic low in the Yellow Sea and western SOJ but not along the overpass path. These examples illustrate that $\overline{\Delta T}_{\text{sea-850}} \geq 13$ °C serves as an effective but imperfect sea-effect discriminator, with non-sea-effect processes contributing to cloud and precipitation development in some situations.

Low cloud occurrence during PSEPs is based on profiles in which clouds are confined to <5 km mean sea level (MSL; Wang et al., 2013) with no clouds in the range ≥5 and ≤8 km MSL (clouds may or may not exist >8 km MSL). This reduces the influence of situations in which deep, likely synoptically forced clouds, may be contributing to precipitation processes. Precipitation occurrence during PSEPs similarly focuses on profiles with these cloud characteristics.

We also present cloud top, radar reflectivity, ice water path (IWP), and liquid water path (LWP) statistics during PSEPs based on Cloudsat- and Aqua-derived products. Cloud tops are obtained from the 2B-RL-GEOPROF product, radar reflectivity from the Geometrical Profile product (2B-GEOPROF; Marchand et al., 2008), IWP from 2C-ICE (Deng et al., 2015), and LWP is derived using the Advanced Microwave Scanning Radiometer-EOS (AMSR-E; Wentz, 1997) and MODIS (Platnick et al., 2003).

Radar reflectivity is susceptible to ground clutter and other noncloud returns, which can impact 2B-GEOPROF products. One approach to combat this issue is to remove all reflectivity values corresponding to 2B-GEOPROF cloud mask values <20 (Marchand et al., 2008). However, ground clutter issues remained after applying this approach in the complex terrain of Japan and Asia (e.g., Figure 4), as observed in other regions (e.g., Kulie et al., 2016; Kulie & Bennartz, 2009; Milani et al., 2015). An

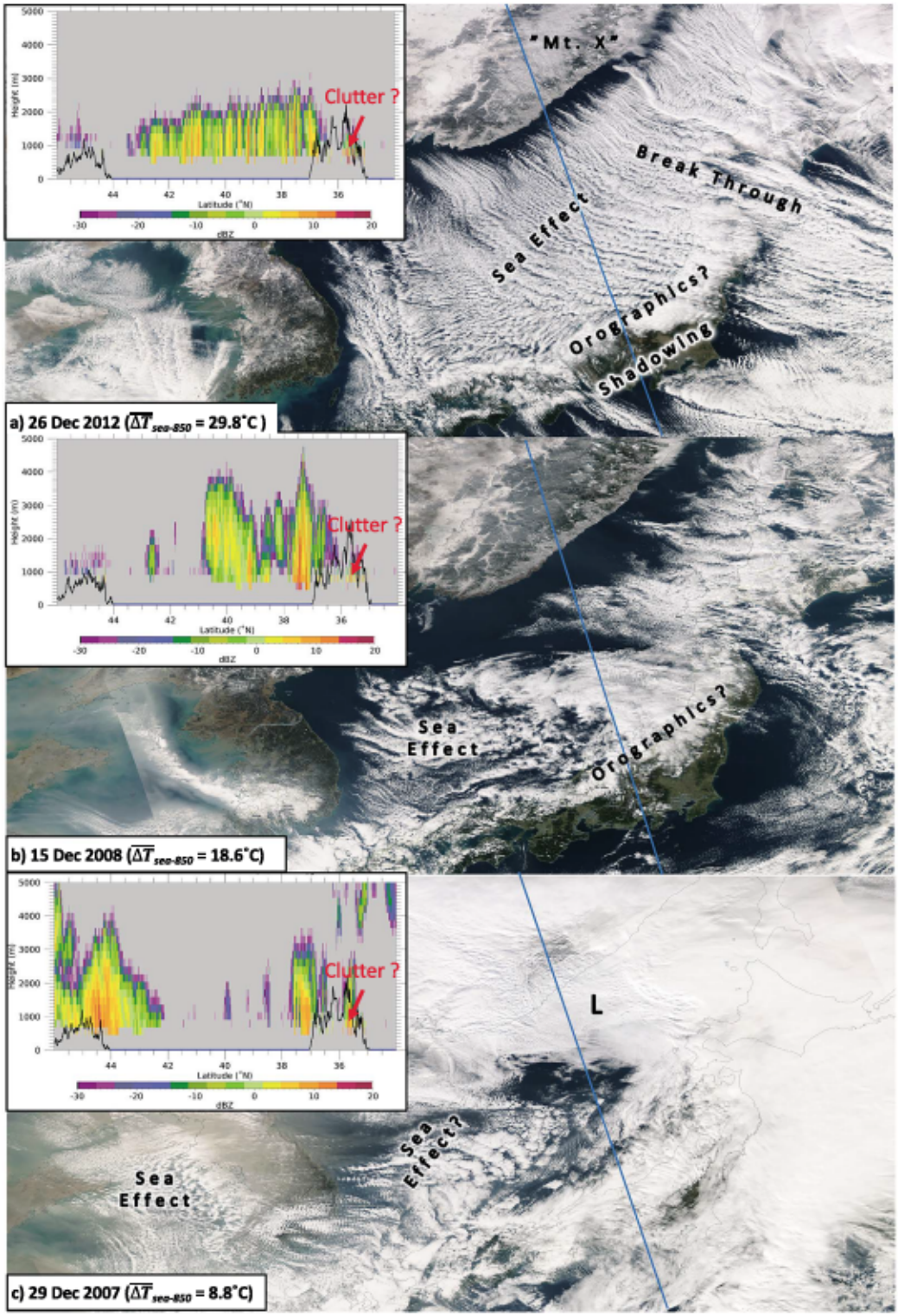

Figure 4. Composite Aqua Moderate Resolution Imaging Spectroradiometer (MODIS) imagery (https://worldview.earthdata.nasa.gov) and Cloudsat cloud profiling radar data for differing synoptic scenarios along a common A-Train orbital track (named *Joetsu* and indicated in blue) for (a) 26 December 2012, (b) 15 December 2008, and (c) 29 December 2007. Cloudsat topography is plotted in black, and reflectivity values below the topography contour show ground clutter.

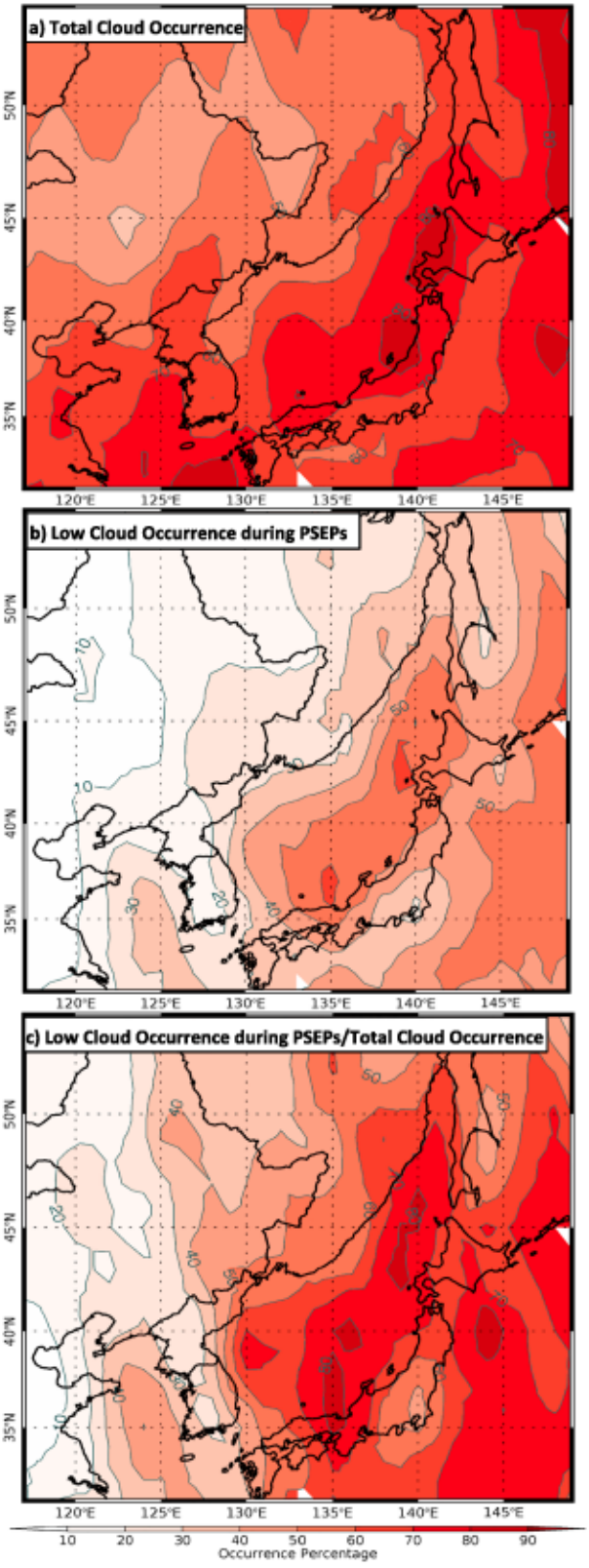

Figure 5. Cloud occurrence expressed as the percentage of Cloudsat profiles containing clouds to total Cloudsat profiles for (a) all clouds during all periods and (b) low clouds during PSEPs. (c) Percentage of low clouds during potential sea-effect periods (PSEPs) to total clouds.

alternative approach for removing clutter is to apply a vertical continuity requirement on the lowest CPR observations (Kulie & Bennartz, 2009), but this can remove a significant portion of shallow snow-producing clouds (Hiley et al., 2011). Based on visual inspection of ground clutter in the SOJ region, we elected to omit reflectivity values <1 km above ground level (AGL) as determined by the Cloudsat digital elevation model (1-km grid spacing). We also eliminated reflectivity values >20 dBZ as these values are above the Cloudsat threshold for snowfall and are likely clutter (Matrosov, 2007; Milani et al., 2015). It should be noted, however, that changes in hydrometeor characteristics and corresponding reflectivity values likely occur below 1 km and are not accounted for here.

3. Regional Cloud and Precipitation Characteristics in the SOJ Region

Air-sea interactions, coastal geometry, and regional terrain strongly modulate patterns of total cloud occurrence in the SOJ region during winter (Figure 5a). Total cloud occurrence increases across the SOJ from Asia to the SOJ coast of Japan where it exceeds 70% north of ~35°N with maxima >80% over the SOJ near the Oki Islands, along the northwest Honshu coast, and along the western Hokkaido coast (Figure 5a). Cloud occurrence declines across Japan and is lower along and offshore the Japanese Pacific coast, consistent with terrain-induced cloud shadowing. Over the SOJ, relatively high cloud occurrence (>70%) is found south of Peter the Great Gulf and east of East Korea Bay where the JPCZ frequently develops. Further west, higher total cloud occurrence values extend northward from the eastern Yellow Sea along the west side of the Korean Highlands. The latter likely reflecting inland and orographic influences.

The occurrence of low clouds during PSEPs exhibits broadly similar patterns but with lower values due to the omission of profiles with midlevel clouds, exclusively high clouds, or periods of $\overline{\Delta T}_{\text{sea-850}} < 13$ °C (Figure 5b). Compared to total cloud occurrence, low-cloud occurrence during PSEPs increases more sharply across the SOJ, reflecting the frequent production of low clouds. Maxima >60% occur just off the SOJ coast of Japan near 135°E and the Oshima Peninsula. Terrain shadowing produces lower values along much of the Pacific coast of Japan, with higher values southeast of the less formidable terrain of the Oshima Peninsula, Tsugaru Strait, and northern Honshu (see also Figure 4a for an example). Beyond the SOJ, a local PSEP low-cloud occurrence maximum (minimum) is found over the Yellow Sea (Korean Peninsula), but there is no evidence of localized cloud production by the Korean Highlands. Overall, low clouds during PSEPs comprise a majority (>50%) of the total cloud occurrence over most of the SOJ, with the lowest contribution (<50%) near the Korean Peninsula and the highest (>70%) in three areas: (1) east of the East Korea Bay, (2) along 135°E (with a secondary maximum just to the northeast near 136°E and 40°N), and (3) between the Asian coast and Hokkaido (Figure 5c).

Consistent with the cloud occurrence patterns described above, total precipitation occurrence increases across the SOJ from the Asian to Japanese coast (Figure 6a). The increase is sharpest over the northern SOJ west of Hokkaido. Values >40% arc from the SOJ near 135°E

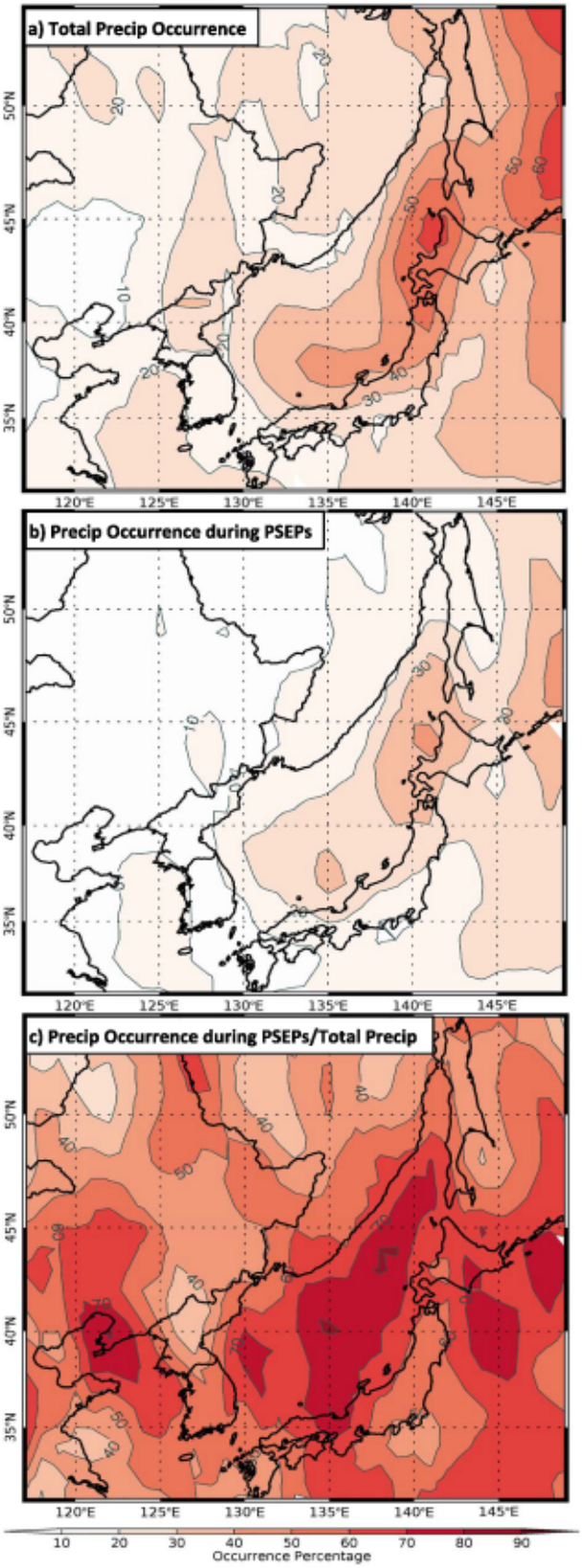

Figure 6. Same as Figure 5 but for precipitation.

and the Oki islands toward Honshu, Hokkaido, and Sakhalin Island, with a maximum >60% near the central west coast of Hokkaido. The increase from central Honshu to Hokkaido is monotonic and more striking than found for cloud occurrence (cf. Figures 5a and 6a). Lower values occur along the Pacific coast of Japan. Further west, low total precipitation occurrence occurs over the southern Korean Peninsula, with higher values over the Yellow Sea and Korean Highlands. Precipitation occurrence during PSEPs exhibits similar patterns, although consistent with low cloud occurrence during PSEPs, there is no maximum over the Korean Highlands (Figure 6b). Precipitation occurrence during PSEPs constitutes over 60% of the total precipitation occurrence over and near the SOJ, with the highest values east of the Korean Peninsula near the JPCZ, along 135°E, and over the SOJ between the Asian coast and the SOJ coasts of Hokkaido and Sakhalin Islands (Figure 6c).

We now focus on PSEPs, beginning with median cloud top, defined as the median of all PSEP cloud top values within a given 1° × 1° latitude-longitude grid box. During PSEPs over the SOJ, median cloud tops generally increase with proximity to the SOJ coasts of Honshu and Hokkaido and are greatest along an arc that extends from the western SOJ and the JPCZ region to the coast of Honshu and then northward to Hokkaido (Figure 7). The highest values (>2,750 m MSL) exist over north-central Honshu, which does not correspond to the location of the highest coastal PSEP precipitation occurrence on the SOJ coast of Hokkaido. The lowest median cloud tops over the SOJ are found near 137°E between the Asian Coast and the Oshima Peninsula. Overall, these results are consistent with increasing cloud depths as sea-effect systems impinge on the Japanese coast and coastal terrain, especially central Honshu.

Next, we summarize PSEP precipitation characteristics with two versions of median near-surface reflectivity using Cloudsat. The first is the standard near-surface reflectivity product from 2C-PRECIP (Figure 8a), which uses the attenuated reflectivity value between 0.6 and 0.84 km AGL (Haynes et al., 2009). The second is an internal calculation we name 1 km AGL, which uses the reflectivity in the lowest CPR bin >1 km AGL (Figure 8b). Medians are calculated using reflectivity values between −35 and 20 dBZ within a given 1° × 1° latitude-longitude grid box. Both versions depict an increase in median reflectivity across the SOJ from the Asian coast to the SOJ coast of Japan and lower values off the Pacific coast of Japan. Over the SOJ, higher values extend northwestward toward the East Korea Bay in the JPCZ region. Maxima in the 2C-PRECIP version exist over central Honshu and along the northwest coast of Hokkaido. In contrast, the 1-km AGL version has no maximum over the former. One contributor to this disparity may be ground clutter in the 2C-PRECIP version over central Honshu, as illustrated in Figure 4 and often observed in CPR data over complex terrain at heights below the .84-km AGL threshold (Kulie et al., 2016). In general, median values are lower for the 1-km AGL version than the 2C-PRECIP version. These differences may reflect the inclusion of ground clutter as well as an increased number of larger hydrometeors (due to more growth time) or unfrozen hydrometeors below 1 km AGL. Beyond the SOJ, both versions produce a maximum over the Yellow Sea near the west coast of the Korean Peninsula.

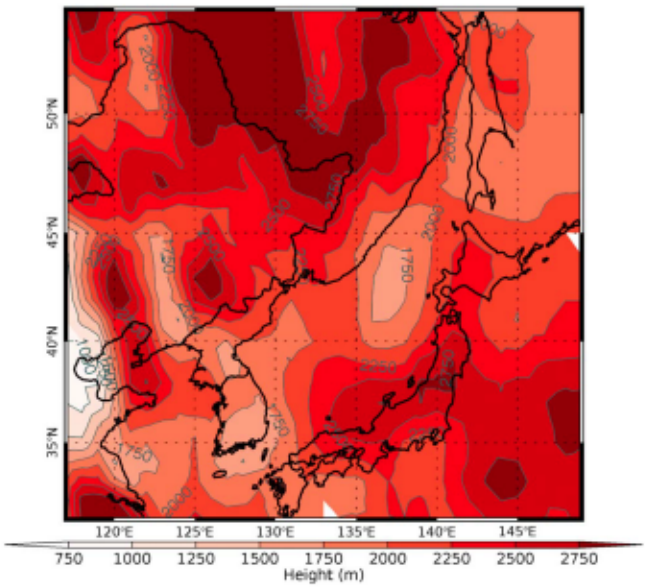

Figure 7. Median cloud top height (m mean sea level) during potential sea-effect periods.

In summary, air-sea interactions, coastal geometry, and regional terrain have strong influences on cloud and precipitation characteristics in the SOJ region. There is a clear increase in total cloud and precipitation occurrence across the SOJ coast from Asia to Japan, with PSEPs contributing a majority (>50%) of the total clouds. Total and PSEP cloud and precipitation occurrence tend to be highest in the western SOJ where the JPCZ frequently develops, along the central and northern SOJ coast of Honshu and along the SOJ coastal area of Hokkaido. Similarly, during PSEPs, cloud tops and median reflectivities are greatest over these regions and the adjoining near-coast topography. Contributions from the convergent areas in the northern SOJ are less pronounced in these Cloudsat derived results. However, when comparing the northern SOJ convergent areas to the central SOJ where no convergence is documented, the northern SOJ convergent areas are categorized by higher cloud frequency near the Asian coast, higher precipitation occurrence, and higher near-surface reflectivity. Of note, some geographic differences exist among the products presented, which in part likely reflects artifacts arising from the interpolation of lattice-like orbital tracks to a relatively course latitude-longitude grid. In addition, such interpolation removes fine-scale cloud and precipitation features near the Japanese coast and adjacent topography. Finally, reflectivity statistics are influenced by the technique used to eliminate ground clutter and may omit important near-surface precipitation processes. As a result, we now focus on cloud and precipitation characteristics along Cloudsat orbital tracks crossing the Asian and Japanese coasts.

4. Along-Track Reflectivity Cross Sections

A-Train derived variables along recurring daytime Cloudsat orbital tracks (hereafter tracks) that cross the SOJ and Japan illustrate the structure and characteristics of clouds and precipitation during PSEPs in greater detail. We identified nine such tracks with names corresponding to a Japanese city along the SOJ coast near each track (Figure 9), but for brevity we present analyses along four tracks that illustrate key cloud and precipitation characteristics observed in the SOJ region. These four tracks are Matsue, Joetsu, Niigata, and Asahikawa. Although these tracks cross the SOJ, they are oriented obliquely to and not directly along the northwesterly surface flow that predominates over the SOJ region during winter (Iizuka, 2010). Each track is displayed with the Asian coast on the left and extends to ~228 km south-southeast of the Japanese SOJ coast, which is at the same location in each plot.

We begin with an analysis of the frequency of radar echoes > −5 dBZ above the 1-km threshold (Figure 10), with the −5-dBZ threshold corresponding to a high confidence of snow (Haynes et al., 2009). Higher reflectivity thresholds exhibit lower frequencies, but similar spatial patterns, as do analyses of ice water content from the Cloudsat 2C-ICE product and snow rate from the Cloudsat 2C-SNOW-PROFILE (not shown). All tracks feature low frequencies over coastal Asia. Along the Matsue track, echo frequencies and depths are greatest over the central SOJ and decline near the Japanese coast, although there is a weak secondary maximum in echo frequency over the adjoining high terrain (Figure 10a). This pattern largely reflects the JPCZ and the influence of the Korean Peninsula, the former serving as a generator of clouds and precipitation over the SOJ and the latter reducing cloud and precipitation occurrence over southern Honshu during westerly to northwesterly flow (see also Figures 5 and 6). A similar pattern is seen in the Tottori track, although the maxima in echo frequency and depth are closer to the coast (not shown).

In contrast, dramatic near coast and inland effects are evident along the Joetsu and Niigata tracks where prominent topography rises near the coast (Figures 10b and 10c). Along each of these tracks, echo frequencies and depths generally increase across the SOJ and peak near the coast and the immediately adjacent topography. Echo frequencies and depths decrease abruptly with inland extent. Similar echo characteristics are evident in the Kyotango and Kanazawa tracks to the west (not shown). Along the Joetsu and Kanazawa tracks, echoes reach greater depths (frequencies >30% extend to 3,000 m MSL) and exhibit a more rapid decline

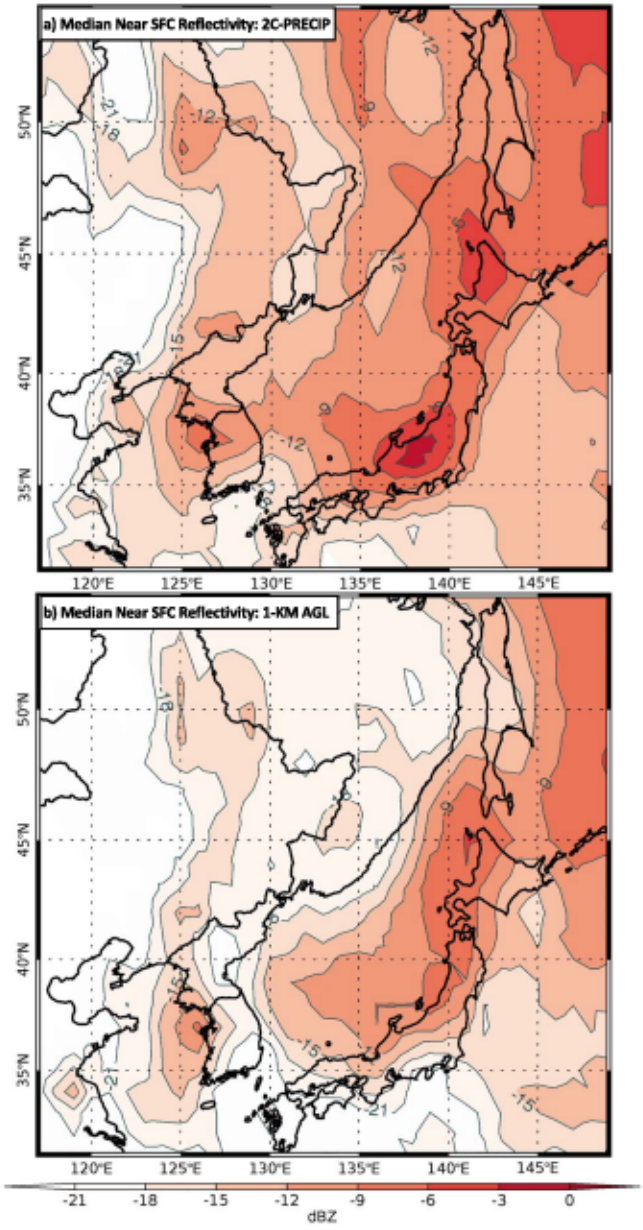

Figure 8. Potential sea-effect period Cloudsat median near-surface reflectivity for (a) 2C-PRECIP and (b) 1-km above ground level.

with inland extent than found along any other tracks (Figure 10b). In addition to inland and orographic effects, the JPCZ often terminates where the Joetsu track intersects the Japanese SOJ coast (e.g., Eito et al., 2010) and may contribute to the near-coast echo frequency maxima. This may also explain the somewhat lower near coast echo frequencies in the Niigata track compared to the Joetsu track.

Over northern Honshu and Hokkaido, the Asahikawa track (Figure 10d) and the Oga and Sapporo tracks (not shown) feature shallower echoes compared to tracks crossing central Honshu, with echo frequencies >30% confined to below ~2,200 m MSL over the SOJ. This result is consistent with the median cloud top height analysis for the SOJ region (Figure 7). However, the Asahikawa track also features the largest area of echo frequencies >45%, resulting in the most frequent precipitation of any track. In addition, offshore echo frequencies are generally higher along these northern tracks, with nearly continuous offshore echo frequencies >30% beginning close to the Asian coast (e.g., within ~115 km for the Asahikawa track), suggesting more rapid and continuous cloud and precipitation development. Changes in echo frequency and depth are less dramatic at the Japanese SOJ coast. While this partially reflects the less continuous and formidable nature of the topography in this region, it also reflects the more oblique orientation of the tracks relative to the coastline.

In summary, radar reflectivity statistics along recurring orbital tracks highlight notable differences in sea-effect storm characteristics over the SOJ region and along the SOJ coast of Japan. The influence of the Korean Peninsula and JPCZ yield an offshore echo frequency maximum along tracks crossing western Honshu. In contrast, tracks crossing the more formidable topography near the SOJ coast of central Honshu feature an echo frequency maximum near the coast or the adjacent coastal topography, with echoes reaching greater depths and exhibiting a more rapid decline with inland extent than found along other tracks. However, additional nonorographic factors may also contribute to this signature, such as the transition from convective to stratiform precipitation (e.g., Minder et al., 2015) and strength of the incident flow (e.g., Veals et al., 2018). In addition, echo frequencies are greatest but confined to lower altitudes, along tracks crossing northern Honshu and Hokkaido. As a result, the most frequent precipitation (northern Honshu and Hokkaido) and the highest cloud tops (central Honshu) occur in different regions. Moreover, Cloudsat 2C-PRECIP near-surface reflectivity (Figure 8a) and precipitation climatologies (e.g., Kawase et al., 2015) infer that central Honshu receives more winter precipitation than Hokkaido, which implies that central Honshu receives less frequent but more intense precipitation.

5. Along-Track Water Paths

We now focus on water paths during PSEPs. LWP (MODIS and AMSR-E) and IWP (2C-ICE) are displayed in Figure 11 for the same four tracks as displayed for reflectivity > −5 dBZ. We examined several other along-track variables including column-summed reflectivity, 1-km AGL reflectivity, 1-km AGL IWC, and surface snow rate, but all exhibit similar qualitative structures and are not presented. Analyzing LWP from the independent MODIS and AMSR-E sensors can produce additional (or less) confidence in Cloudsat-derived findings and can also provide a glimpse into cloud macrophysical and microphysical processes (Hu et al., 2010). MODIS and AMSR-E have larger footprints than Cloudsat, but the data displayed are aligned with the

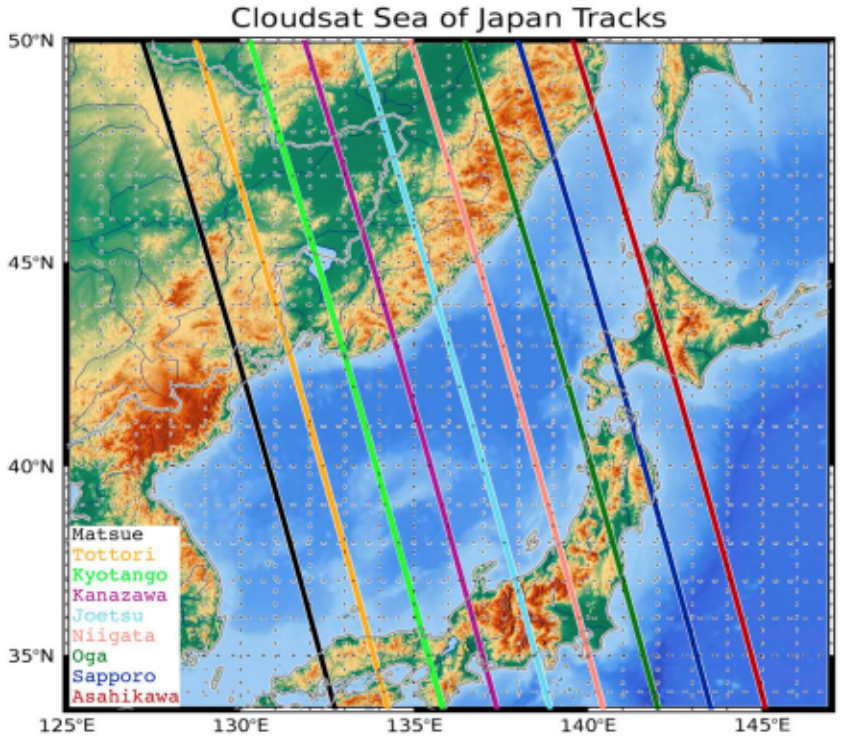

Figure 9. Recurring Cloudsat orbital tracks labeled according to nearby Japanese cities on the Sea of Japan coast.

Cloudsat footprint. Due to a reduced AMSR-E lifespan, only LWP data between January 2007 and February 2011 are displayed. Since AMSR-E uses microwave radiometers that depend on constant emissivity, only AMSR-E data over nonshallow water are available. Uncertainty exists among the three retrieved water path products. Khanal and Wang (2018) found a 15–40% MODIS LWP bias for mixed-phase clouds.

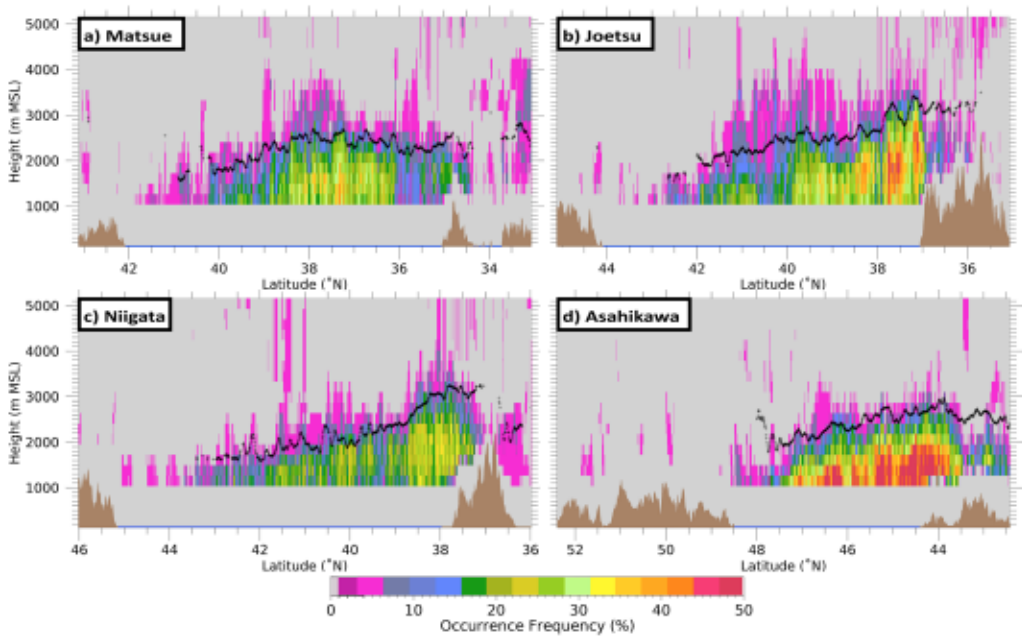

Figure 10. Frequency of reflectivity > −5 dBZ for potential sea-effect periods profiles along the (a) Matsue, (b) Joetsu, (c) Niigata, and (d) Asahikawa tracks. Cloudsat digital elevation model terrain is plotted in brown, and median cloud top height from 2B-RL-GEOPROF is plotted in black where sufficient data exist.

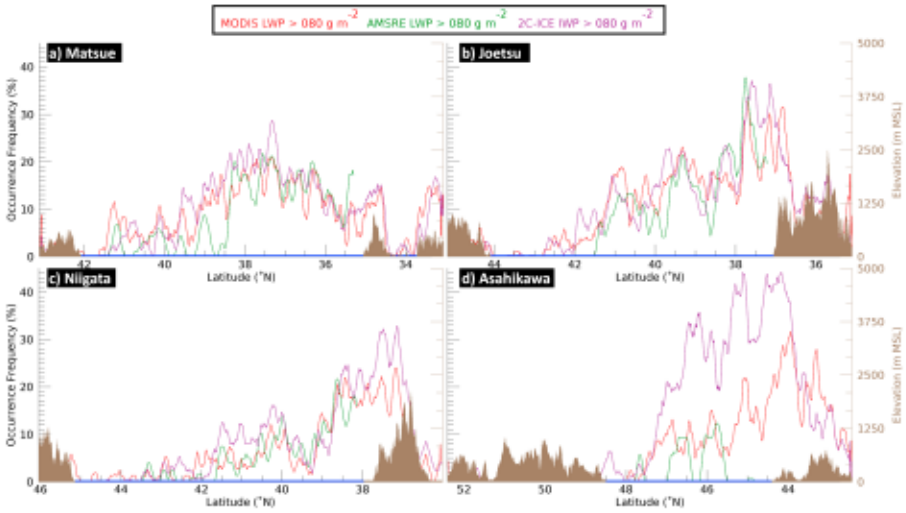

Figure 11. Frequency of Moderate Resolution Imaging Spectroradiometer (MODIS) liquid water path (LWP) > 80 g/m^2 (red), Advanced Microwave Scanning Radiometer-EOS (AMSR-E) LWP > 80 g/m^2 (green), and 2C-ICE ice water path (IWP) > 80 g/m^2 (purple) for potential sea-effect period profiles along the (a) Matsue, (b) Joetsu, (c) Niigata, and (d) Asahikawa tracks. Cloudsat digital elevation model terrain is plotted in brown.

AMSR-E can be biased high compared to MODIS but is considered advantageous due to microwave emissions from liquid water being available throughout the column (Lebsock & Su, 2014). Uncertainties of 30% have been found for 2C-ICE ice water and are mostly related to assumptions regarding ice particle habit (Deng et al., 2013, 2015). We focus on the frequency of LWP and IWP ≥ 80 g/m^2, which is typical of water path values for this region and season (Heng et al., 2014). LWP and IWP thresholds of 60 and 100 g/m^2 were also analyzed, and while the frequency of occurrence increases and decreases respectively, they exhibit nearly identical qualitative trends (not shown). Both LWP and IWP are smoothed using a boxcar average with a width of 7.

For individual tracks, the Matsue track shows a maximum for LWP and IWP frequency over the central SOJ and a decrease toward the Japanese SOJ coast that is consistent with reflectivity cross sections (cf. Figures 10a and 11a). In contrast, the Joetsu and Niigata tracks reach their highest LWP and IWP values close to the Japanese SOJ coast, although the maximum in LWP and IWP is along the coast for the Joetsu track and further inland for the Niigata track. The Niigata track also has lower overall frequency values, which was noted in the reflectivity cross-section results and may be due to the propensity of the JPCZ to terminate closer to Joetsu (Eito et al., 2010) or upstream precipitation shadowing by a coastal island.

Compared to other tracks, the Asahikawa track exhibits much higher IWP frequencies but similar LWP frequencies over the SOJ (Figure 11d). Although not shown, median IWP and median IWC are also greater along the Asahikawa track, indicating greater volumetric ice concentrations. This is another example of differences between the Hokkaido tracks and those over central Honshu, hinting at differences in precipitation formation processes. These differences in ice properties may reflect lower temperatures over the northern SOJ or differences in storm dynamics and microphysics not examined here.

In summary, PSEP passive LWP and active IWP qualitative patterns are very similar to those derived from reflectivity measurements. While uncertainties exist in LWP and IWP retrievals, the uncertainties appear less applicable to our data set given the general agreement between LWP, IWP, and reflectivity. This agreement indicates either low bias within our data set or that LWP, IWP, and reflectivity have the same bias, with the latter being unlikely. Uncertainty is also mitigated by focusing on overall trends and patterns and by using frequency of occurrence versus actual numerical values. The similarities between passive and active sensors also strengthen the overall findings of the reflectivity data in sections 4 and 5, such as differences between the Joetsu and Niigata tracks and more frequent precipitation over the northern SOJ. In addition, frozen hydrometeors (IWP > 80 g/m^2) occur much more frequently along the Asahikawa track despite similar frequencies of LWP > 80 g/m^2, hinting at increased ice concentrations and different microphysical processes compared to the central and southern SOJ.

6. Conclusions

The results of this study show that the preponderance of winter clouds and precipitation in the SOJ region occurs during PSEPs and that sea-effect clouds and precipitation are strongly influenced by land-sea interactions, coastline geometry, and orographic effects. Clouds and precipitation during all periods and PSEPs generally increase from northwest to southeast across the SOJ and maximize along the Japanese SOJ coast or near-coastal terrain. Additional cloud and precipitation frequency maxima occur in the JPCZ and off the coast of Hokkaido, resulting in an arc-like shape of maximum cloud and precipitation frequency from the southwest SOJ to the Honshu coast and northward to Hokkaido. The JPCZ region features more frequent PSEP clouds and precipitation, deeper clouds, and more frequent near-surface precipitation compared to the surrounding area. This confirms the hypothesis that the JPCZ plays an important role in cloud and precipitation production. Cloud and precipitation frequency are higher in the northern SOJ compared to the surrounding area, but the influence of northern convergent zones (e.g., Katsumata et al., 1998; Muramatsu, 1979; Ohtake et al., 2009) on PSEP clouds and precipitation was not apparent in this analysis, perhaps due to limitations in spatial resolution, interpolation, and sample size.

The orography along the Japanese SOJ coast plays a key role in modulating sea-effect clouds and precipitation. This is demonstrated by a maximum in precipitation occurrence and median near-surface reflectivity values along the Japanese SOJ coast, which occurs near the coast even as the SOJ fetch varies from 550 to 850 km. This maximum is often ascribed to coastal, inland, and orographic effects (Campbell & Steenburgh, 2017; Nakai & Endoh, 1995; Saito et al., 1996; Veals & Steenburgh, 2015). Orographic influences also likely contribute to a lowering of echo tops and a sharp decrease in cloud and precipitation frequency with inland extent and to the lee of mountain barriers. These effects are most pronounced downstream of higher mountain barriers. While we highlight the connection between the formidable topography and inland penetration of clouds and precipitation, other factors may influence the inland penetration including the velocity of the incident flow (e.g., Veals et al., 2018) and the depth of the boundary layer coupled with the strength of cold air advection near the top of the boundary layer (e.g., Eipper et al., 2018).

Distinct differences in cloud and precipitation characteristics exist along Cloudsat tracks bisecting the Japanese SOJ coast. The Matsue track intersecting southern Honshu has a clear maximum in cloud and precipitation frequency upstream of the Japanese coast, which reflects the generation of clouds by the JPCZ and more limited cloud production downstream of the Korean Peninsula. Tracks intersecting central Honshu have the longest fetch and highest cloud tops but observe precipitation less frequently than tracks intersecting Hokkaido. Comparing the Joetsu and Niigata tracks of central Honshu also demonstrates differences in inland precipitation penetration that appear to be related to contrasts in terrain height. Differences in IWP statistics between central Honshu and Hokkaido tracks also indicate that the latter features greater volumetric ice concentrations despite similar LWPs, indicating different cloud properties and microphysical processes operating in the two regions.

This work illustrates the important characteristics of sea effect in the SOJ region, but further study is needed to fully investigate why cloud and precipitation properties vary between central Honshu and Hokkaido regions. Additional study is also needed to diagnose precipitation differences between the coastal regions of Joetsu and Niigata. The important climatological role of the JPCZ has been noted here, and future research regarding the synoptic and macrophysical influences on JPCZ formation, location, and strength would enhance understanding and prediction of this feature.

Acknowledgments
All CloudSat and meteorological data used for this work were acquired from the CloudSat Data Processing Center at the Colorado State University (http://www.cloudsat.cira.colostate.edu). MODIS and AMSR-E data were obtained from NASA's Distributed Active Archive Centers (https://ladsweb.modaps.eosdis.nasa.gov/archive/ and https://nsidc.org/data/amsre). Insightful comments from Sento Nakai and two anonymous reviewers along with suggestions or assistance from Steven Krueger, A. Gannet Hallar, Jeremy Gibbs, Adam Abernathy, Sally Benson, Peter Veals, Tom Gowan, and Leah Campbell greatly enhanced this work. We acknowledge the efforts of the engineers and scientists at the Jet Propulsion Laboratory, Ball Aerospace, and the Cooperative Institute for Research in the Atmosphere (CIRA) at the Colorado State University for making the CloudSat project successful. We thank the University of Utah Center for High Performance Computing for the storage and provision of data sets and/or software. This research is based in part on work supported by National Science Foundation grant AGS-1635654 and NASA grants NNX13AQ34G, NNX10AM42G, NNX15AK17G, and NNX13A169G. The first author is supported by the U.S. Air Force Institute of Technology (AFIT) and recognizes AFIT's key role in this work. The opinions, findings, recommendations, and conclusions expressed in this article are those of the authors and do not reflect the official policy or position of the University of Utah, National Science Foundation, NASA, U.S. Air Force, Department of Defense, or the U.S. Government.

References

Andersson, T., & Nilsson, S. (1990). Topographically inducted convective snowbands over the Baltic Sea and their precipitation distribution. *Weather and Forecasting, 5*(2), 299–312. https://doi.org/10.1175/1520-0434(1990)005<0299:TICSOT>2.0.CO;2

Boyle, J., & Chen, T. J. (1987). Synoptic aspects of the wintertime East Asian monsoon. In C. P. Chang & T. N. Krishnamurti (Eds.), *Monsoon meteorology* (pp. 125–160). New York, NY: Oxford University Press.

Campbell, L. S., & Steenburgh, W. J. (2017). The OWLeS IOP2b lake-effect snowstorm: Mechanisms contributing to the Tug Hill precipitation maximum. *Monthly Weather Review, 145*(7), 2461–2478. https://doi.org/10.1175/MWR-D-16-0461.1

Campbell, L. S., Steenburgh, W. J., Yamada, Y., Kawashima, M., & Fujiyoshi, Y. (2018). Influences of orography and coastal geometry on a transverse-mode sea-effect snowstorm over Hokkaido Island, Japan. *Monthly Weather Review, 146*(7), 2201–2220. https://doi.org/10.1175/MWR-D-17-0286.1

Chechin, D. G., & Pichugin, M. K. (2015). Cold-air outbreaks over the ocean at high latitudes and associated mesoscale atmospheric circulations: Problems of numerical modelling. *Izvestiya, Atmospheric and Oceanic Physics, 51*(9), 1034–1050. https://doi.org/10.1134/S0001433815090078

Deng, M., Mace, G. G., Wang, Z., & Berry, E. (2015). CloudSat 2C-ICE product update with a new Ze parameterization in lidar-only region. *Journal of Geophysical Research: Atmospheres*, *120*, 12,198–12,208. https://doi.org/10.1002/2015JD023600

Deng, M., Mace, G. G., Wang, Z., & Lawson, R. P. (2013). Evaluation of several A-Train ice cloud retrieval products with in situ measurements collected during the SPARTICUS campaign. *Journal of Applied Meteorology and Climatology*, *52*(4), 1014–1030. https://doi.org/10.1175/JAMC-D-12-054.1

Dorman, C. E., Beardsley, R. C., Dashko, N. A., Friehe, C. A., Kheilf, D., Cho, K., et al. (2004). Winter marine atmospheric conditions over the Japan Sea. *Journal of Geophysical Research*, *109*, C12011. https://doi.org/10.1029/2001JC001197

Eipper, D. T., Young, G. S., Greybush, S. J., Saslo, S., Sikora, T. D., & Clark, R. D. (2018). Predicting the inland penetration of Long-Lake-Axis-Parallel snowbands. *Weather and Forecasting*, *33*(5), 1435–1451. https://doi.org/10.1175/WAF-D-18-0033.1

Eito, H., Kato, T., Yoshizaki, M., & Adachi, A. (2005). Numerical simulation of the quasi-stationary snowband observed over the southern coastal area of the Sea of Japan on 16 January 2001. *Journal of the Meteorological Society of Japan*, *83*(4), 551–576. https://doi.org/10.2151/jmsj.83.551

Eito, H., Murakami, M., Muroi, C., Kato, T., Hayashi, S., & Kuroiwa, H. (2010). The structure and formation mechanism of transversal cloud bands associated with the Japan-Sea Polar-Airmass Convergence Zone. *Journal of the Meteorological Society of Japan*, *88*(4), 625–648. https://doi.org/10.2151/jmsj.2010-402

Estoque, M. A., & Ninomiya, K. (1976). Numerical simulation of Japan Sea effect snowfall. *Tellus*, *28*, 3.

Haynes, J. M., L'Ecuyer, T. S., Stephens, G. L., Miller, S. D., Mitrescu, C., Wood, N. B., & Tanelli, S. (2009). Rainfall retrieval over the ocean with spaceborne W-band radar. *Journal of Geophysical Research*, *114*, D00A22. https://doi.org/10.1029/2008JD009973

Heng, Z., Fu, Y., Liu, G., Zhou, R., Wang, Y., Yuan, R., et al. (2014). A study of the distribution and variability of cloud water using ISCCP, SSM/I cloud product, and reanalysis datasets. *Journal of Climate*, *27*(9), 3114–3128. https://doi.org/10.1175/JCLI-D-13-00031.1

Hiley, M. J., Kulie, M. S., & Bennartz, R. (2011). Uncertainty analysis for CloudSat snowfall retrievals. *Journal of Applied Meteorology and Climatology*, *50*(2), 399–418. https://doi.org/10.1175/2010JAMC2505.1

Holroyd, E. W. (1971). Lake-effect cloud bands as seen from weather satellites. *Journal of Atmospheric Sciences*, *28*(7), 1165–1170. https://doi.org/10.1175/1520-0469(1971)028<1165:LECBAS>2.0.CO;2

Hozumi, K., & Magono, C. (1984). The cloud structure of convergent cloud bands over the Japan Sea in winter monsoon period. *Journal of the Meteorological Society of Japan*, *62*(3), 522–533. https://doi.org/10.2151/jmsj1965.62.3_522

Hu, Y., Rodier, S., Xu, K., Sun, W., Huang, J., Lin, B., et al. (2010). Occurrence, liquid water content, and fraction of supercooled water clouds from combined CALIOP/IIR/MODIS measurements. *Journal of Geophysical Research*, *115*, D00H34. https://doi.org/10.1029/2009JD012384

Igel, M. R., Drager, A. J., & van den Heever, S. C. (2014). A CloudSat cloud object partitioning technique and assessment and integration of deep convective anvil sensitivities to sea surface temperature. *Journal of Geophysical Research: Atmospheres*, *119*, 515–535. https://doi.org/10.1002/2014JD021717

Iizuka, S. (2010). Simulations of wintertime precipitation in the vicinity of Japan: Sensitivity to fine-scale distributions of sea surface temperature. *Journal of Geophysical Research*, *115*, D10107. https://doi.org/10.1029/2009JD012576

Im, E., Durden, S. L., & Wu, C. (2005). Cloud profiling radar for the CloudSat mission. *IEEE Aerospace and Electronic Systems Magazine*, *20*(10), 15–18. https://doi.org/10.1109/MAES.2005.1581095

Katsumata, M., Uyeda, H., & Kikuchi, K. (1998). Characteristics of a cloud band off the west coast of Hokkaido Island as determined from AVHRR/NOAA, SSM/I and radar data. *Journal of the Meteorological Society of Japan*, *76*(2), 169–189. https://doi.org/10.2151/jmsj1965.76.2_169

Kawamoto, T. S., Miyazawa, S., & Fuj, K. (1963). Heavy Snowfalls Caused by the Hokuriku Front. *Kisho-kenkyu Note*, *14*, 56–70.

Kawase, H., Sasaki, H., Murata, A., Nosaka, M., & Ishizaki, N. N. (2015). Future changes in winter precipitation around Japan projected by ensemble experiments using NHRCM. *Journal of the Meteorological Society of Japan*, *93*(5), 571–580. https://doi.org/10.2151/jmsj.2015-034

Khanal, S., & Wang, Z. (2018). Uncertainties in MODIS-based cloud liquid water path retrievals at high latitudes due to mixed-phase clouds and cloud top height inhomogeneity. *Journal of Geophysical Research:Atmospheres*, *123*, 11,154–11,172. https://doi.org/10.1029/2018JD028558

Kindap, T. (2010). A severe sea-effect snow episode over the city of Istanbul. *Natural Hazards*, *54*(3), 707–723. https://doi.org/10.1007/s11069-009-9496-7

Kristovich, D. A., Clark, R. D., Frame, J., Geerts, B., Knupp, K. R., Kosiba, K. A., et al. (2017). The Ontario Winter Lake-effect Systems (OWLeS) field campaign: Scientific and educational adventures to further our knowledge and prediction of lake-effect storms. *Bulletin of the American Meteorological Society*, *98*(2), 315–332. https://doi.org/10.1175/BAMS-D-15-00034.1

Kulie, M. S., & Bennartz, R. (2009). Utilizing spaceborne radars to retrieve dry snowfall. *Journal of Applied Meteorology and Climatology*, *48*(12), 2564–2580. https://doi.org/10.1175/2009JAMC2193.1

Kulie, M. S., Milani, L., Wood, N. B., Tushaus, S. A., Bennartz, R., & L'Ecuyer, T. S. (2016). A shallow cumuliform snowfall census using spaceborne radar. *Journal of Hydrometeorology*, *17*(4), 1261–1279. https://doi.org/10.1175/JHM-D-15-0123.1

Kusunoki, K., Murakami, M., Orikasa, N., Hoshimoto, M., & Tanaka, Y. (2005). Observations of quasi-stationary and shallow orographic snow clouds: Spatial distributions of supercooled liquid water and snow particles. *Monthly Weather Review*, *133*(4), 743–751. https://doi.org/10.1175/MWR2874.1

Laird, N. F., Desrochers, J., & Payer, M. (2009). Climatology of lake-effect precipitation events over Lake Champlain. *Journal of Applied Meteorology and Climatology*, *48*(2), 232–250. https://doi.org/10.1175/2008JAMC1923.1

Lebsock, M., & Su, H. (2014). Application of active spaceborne remote sensing for understanding biases between passive cloud water path retrievals. *Journal of Geophysical Research: Atmospheres*, *119*, 8962–8979. https://doi.org/10.1002/2014JD021568

Mace, G. G., & Zhang, Q. (2014). The CloudSat radar-lidar geometrical profile product (RL-GeoProf): Updates, improvements, and selected results. *Journal of Geophysical Research: Atmospheres*, *119*, 9441–9462. https://doi.org/10.1002/2013JD021374

Mace, G. G., Zhang, Q., Vaughan, M., Marchand, R., Stephens, G., Trepte, C., & Winker, D. (2009). A description of hydrometeor layer occurrence statistics derived from the first year of merged Cloudsat and CALIPSO data. *Journal of Geophysical Research*, *114*, D00A26. https://doi.org/10.1029/2007JD009755

Magono, C., Kikuchi, K., Kimura, T., Tazawa, S., & Kasai, T. (1966). A study of the snowfall in the winter monsoon season in Hokkaido with special reference to low land snowfall. *Journal of Faculty of Science Hokkaido University*, *2*(3), 287–308.

Marchand, R. T., Mace, G. G., & Ackerman, T. P. (2008). Hydrometeor detection using CloudSat: An Earth orbiting 94 GHz cloud radar. *Journal of Atmospheric and Oceanic Technology*, *25*(4), 519–533. https://doi.org/10.1175/2007JTECHA1006.1

Matrosov, S. Y. (2007). Modeling backscatter properties of snowfall at millimeter wavelengths. *Journal of Atmospheric Science*, *64*(5), 1727–1736. https://doi.org/10.1175/JAS3904.1

Milani, L., Porcù, F., Casella, D., Dietrich, S., Panegrossi, G., Petracca, M., & Sanò, P. (2015). Analysis of long-term precipitation pattern over Antarctica derived from satellite-borne radar. *Cryosphere Discussions*, *9*(1), 141–182. https://doi.org/10.5194/tcd-9-141-2015

Minder, J. R., Letcher, T. W., Campbell, L. S., Veals, P. V., & Steenburgh, W. J. (2015). The evolution of lake-effect convection during landfall and orographic uplift as observed by profiling radars. *Monthly Weather Review*, *143*(11), 4422–4442. https://doi.org/10.1175/MWR-D-15-0117.1

Mitnik, L. M. (1992). Mesoscale coherent structures in the surface wind field during cold air outbreaks over the Far Eastern seas from the satellite side looking radar. *La Mer*, *30*, 287–296.

Mizukoshi, M. (1977). Climatic division and climatography. In E. Fukui (Ed.), *The climate of Japan* (pp. 225–270). Kodansha, Tokyo: Elsevier.

Murakami, M., Clark, T. L., & Hall, W. D. (1994). Numerical simulations of convective snow clouds over the Sea of Japan; two-dimensional simulations of mixed layer development and convective snow cloud formation. *Journal of the Meteorological Society of Japan*, *72*(1), 43–62. https://doi.org/10.2151/jmsj1965.72.1_43

Muramatsu, T. (1979). The cloud line enhanced by upwind orographic features in winter monsoon situations. *Geophysical Magazine*, *38*, 1–15.

Nagata, M. (1987). On the formation of a convergent cloud band over the Japan Sea in winter: A prediction experiment. *Journal of the Meteorological Society of Japan*, *65*(6), 871–883. https://doi.org/10.2151/jmsj1965.65.6_871

Nagata, M. (1991). Further numerical study on the formation of the convergent cloud band over the Japan Sea in winter. *Journal of the Meteorological Society of Japan*, *69*(3), 419–428. https://doi.org/10.2151/jmsj1965.69.3_419

Nagata, M., Ikawa, M., Yoshizumi, S., & Yoshida, T. (1986). On the formation of a convergent cloud band over the Japan Sea in winter; numerical experiments. *Journal of the Meteorological Society of Japan*, *64*(6), 841–855. https://doi.org/10.2151/jmsj1965.64.6_841

Nakai, S., & Endoh, T. (1995). Observation of snowfall and airflow over a low mountain barrier. *Journal of the Meteorological Society of Japan*, *73*(2), 183–199. https://doi.org/10.2151/jmsj1965.73.2_183

Nakai, S., Iwanami, K., Misumi, R., Park, S. G., & Kobayahsi, T. (2005). A classification of snow clouds by Doppler radar observations at Nagaoka, Japan. *Science Online Letters on the Atmosphere*, *1*, 161–164. https://doi.org/10.2151/sola.2005-042

Nakai, S., Sato, T., Sato, A., Hirashima, H., Nemoto, M., & Motoyoshi, H. (2012). A Snow Disaster Forecasting System (SDFS) constructed from field observations and laboratory experiments. *Cold Regions Science and Technology*, *70*, 53–61. https://doi.org/10.1016/j.coldregions.2011.09.002

Niziol, T. A. (1987). Operational forecasting of lake effect snowfall in western and central New York. *Weather and Forecasting*, *2*(4), 310–321. https://doi.org/10.1175/1520-0434(1987)002<0310:OFOLES>2.0.CO;2

Niziol, T. A., Snyder, W. R., & Waldstreicher, W. R. (1995). Winter weather forecasting throughout the eastern United States. Part IV: Lake effect snow. *Weather and Forecasting*, *10*(1), 61–77. https://doi.org/10.1175/1520-0434(1995)010<0061:WWFTTE>2.0.CO;2

Norris, J., Vaughan, G., & Schultz, D. M. (2013). Snowbands over the English Channel and Irish Sea during cold-air outbreaks. *Quarterly Journal of the Royal Meteorological Society*, *139*(676), 1747–1761. https://doi.org/10.1002/qj.2079

Ohtake, H., Kawashima, M., & Fujiyoshi, Y. (2009). The formation mechanism of a thick cloud band over the northern part of the Sea of Japan during cold air outbreaks. *Journal of the Meteorological Society of Japan*, *87*(2), 289–306. https://doi.org/10.2151/jmsj.87.289

Partain, P. (2007). CloudSat ECMWF-AUX auxiliary data process description and interface control document, *Cooperative Institute for Research in the Atmosphere Technical Report 5.2*, 10 pp., Colorado State University, Fort Collins.

Platnick, S., King, M. D., Ackerman, S. A., Menzel, W. P., Baum, B. A., Riedi, J. C., & Frey, R. A. (2003). The MODIS cloud products: Algorithms and examples from Terra. *IEEE Transactions on Geoscience and Remote Sensing*, *41*(2), 459–473. https://doi.org/10.1109/TGRS.2002.808301

Saito, K., Murakami, M., Matsuo, T., & Mizuno, H. (1996). Sensitivity experiments on the orographic snowfall over the mountainous region of northern Japan. *Journal of the Meteorological Society of Japan*, *74*(6), 797–813. https://doi.org/10.2151/jmsj1965.74.6_797

Steenburgh, W. J. (2014). *Secrets of the greatest snow on Earth* (p. 186). Logan, Utah: Utah State University Press.

Steenburgh, W. J., Halvorson, S. F., & Onton, D. J. (2000). Climatology of lake-effect snowstorms of the Great Salt Lake. *Monthly Weather Review*, *128*(3), 709–727. https://doi.org/10.1175/1520-0493(2000)128<0709:COLESO>2.0.CO;2

Stephens, G. L., Vane, D. G., Boain, R. J., Mace, G. G., Sassen, K., Wang, Z., et al., & The CloudSat Science Team (2002). The CloudSat mission and the A-Train. *Bulletin of the American Meteorological Society*, *83*(12), 1771–1790. https://doi.org/10.1175/BAMS-83-12-1771

Takahashi, H. G., Ishizaki, N. H., Kawase, H., Hara, M., Yoshikane, T., Ma, X., & Kimura, F. (2013). Potential impact of sea surface temperature on winter precipitation over the Sea of Japan side of Japan: A regional climate modeling study. *Journal of the Meteorological Society of Japan*, *91*(4), 471–488. https://doi.org/10.2151/jmsj.2013-404

Tanelli, S., Durden, S. L., Im, E., Pak, K. S., Reinke, D. G., Partain, P., et al. (2008). CloudSat's cloud profiling radar after two years in orbit: Performance, calibration, and processing. *IEEE Transactions on Geoscience and Remote Sensing*, *46*(11), 3560–3573. https://doi.org/10.1109/TGRS.2008.2002030

Tsuchiya, K., & Fujita, T. (1967). A satellite meteorological study of evaporation and cloud formation over the western Pacific under the influence of the winter monsoon. *Journal of the Meteorological Society of Japan*, *45*(3), 232–250. https://doi.org/10.2151/jmsj1965.45.3_232

Veals, P. G., & Steenburgh, W. J. (2015). Climatological characteristics and orographic enhancement of lake-effect precipitation east of Lake Ontario and over the tug hill plateau. *Monthly Weather Review*, *143*(9), 3591–3609. https://doi.org/10.1175/MWR-D-15-0009.1

Veals, P. G., Steenburgh, W. J., & Campbell, L. S. (2018). Factors affecting the inland and orographic enhancement of lake-effect precipitation over the Tug Hill Plateau. *Monthly Weather Review*, *146*, 1745–1762. https://doi.org/10.1175/MWR-D-17-0385.1

Wang, Y., Liu, G., Seo, E.-K., & Fu, Y. (2013). Liquid water in snowing clouds: Implications for satellite remote sensing of snowfall. *Atmospheric Research*, *131*, 60–72. https://doi.org/10.1016/j.atmosres.2012.06.008

Wentz, F. J. (1997). A well-calibrated ocean algorithm for SSM/I. *Journal of Geophysical Research*, *102*(C4), 8703–8718. https://doi.org/10.1029/96JC01751

Winker, D. M., Pelon, J. R., & McCormick, M. P. (2003). The CALIPSO mission: Spaceborne lidar for observation of aerosols and clouds. *Proceedings SPIE International Society for Optics and Photonics*, *4893*, 1–11. https://doi.org/10.1117/12.466539

Yamaguchi, S., Abe, O., Nakai, S., & Sato, A. (2011). Recent fluctuations of meteorological and snow conditions in Japanese mountains. *Annals of Glaciology*, *52*(58), 209–215. https://doi.org/10.3189/172756411797252266

Yoshihara, H., Kawashima, M., Arai, K., Inoue, J., & Fujiyoshi, Y. (2004). Doppler radar study on the successive development of snowbands at a convergence line near the coastal region of Hokuriku District. *Journal of the Meteorological Society of Japan*, *82*(4), 1057–1079. https://doi.org/10.2151/jmsj.2004.1057